

Optical reflection signature of an axion dielectric with magnetic current

Pedro D. S. Silva^{a,*}, Ronald A. Pereira^{a,†} and Manoel M. Ferreira Jr.^{a,b,‡}

^a*Programa de Pós-graduação em Física, Universidade Federal do Maranhão, Campus Universitário do Bacanga, São Luís (MA), 65080-805, Brazil and*

^b*Departamento de Física, Universidade Federal do Maranhão, Campus Universitário do Bacanga, São Luís (MA), 65080-805, Brazil*

In this work, we investigate the reflection properties on the interface between an ordinary dielectric medium and a dielectric supporting a magnetic current (equivalent to a dielectric governed by axion electrodynamics). Considering the usual Maxwell equations and constitutive relations, we derive the general Fresnel coefficients for reflection for an incident wave with s and p polarization, assuming an isotropic magnetic current on a dielectric substrate. We determine all total internal reflection and critical angles (Brewster angles) conditions, which are given by strict relations between all relevant electromagnetic quantities of the system and the frequency. For s - and p -polarized incident waves, total internal reflection can occur under certain conditions on the constitutive parameters (for each propagating mode) at specific frequency windows and certain incidence angle intervals. All possible conditions to define critical angles for null reflection are determined. This scenario allows polarization changes by reflection. Considering a p -polarized incident wave, the frequency and the Brewster angle, allowing null reflection for both propagating modes, are determined. The Goos-Hänchen shift and the complex Kerr rotation are also evaluated. The Kerr ellipticity angle presents a frequency-dependent behavior, also reported in Weyl semimetals, having maximum values $\eta_{Kerr} = \pm\pi/4$ for specific values of frequency, which may work as a signature of this axion chiral dielectric.

PACS numbers: 41.20.Jb, 78.20.Ci, 78.20.Fm

I. INTRODUCTION

When light impinges on the interface between two distinct media, the reflection and transmission properties are given by the Fresnel coefficients derived from the Maxwell equations, constitutive relations, and boundary conditions [1, 2]. This procedure is also applied for interfaces between non-usual media, such as the ones separating bi-isotropic dielectrics [3, 4] and topological insulators [5], for which the polarization rotation at the Brewster angle may provide a convenient way to determine the magnitude of the chiral coupling [5]. A similar investigation in interfaces between topological and left-handed metamaterials revealed the possibility of designing a perfect lens [6].

Electromagnetic properties of distinct materials can be expressed in terms of optical quantities, such as the Kerr rotation for the reflected wave, the Goos-Hänchen shift, and birefringence effects. Chiral media, marked by optical activity, are also characterized by the rotatory power (RP), which measures the polarization rotation associated with birefringence [7]. The RP is useful to measure the Faraday effect in crystals [8] and plasmas [9], as well as to describe crystals [11, 12], organic compounds [13, 14], graphene phenomena at terahertz band [15], gas of fast-spinning molecules [16], chiral metamaterials [17–19], and chiral semimetals [20, 21]. In some particular

systems where the RP depends on the frequency, it may undergo sign reversion, which is a feature of rotating plasmas [22, 23], chiral cold plasmas [24, 25], and bi-isotropic media with chiral magnetic current [26].

Light reflection on matter surfaces is a useful technique to examine features of distinct materials, including the generation of circularly polarized (CP) and elliptically polarized (EP) waves (not usually available in nature), caused by reflection from materials with a complex refractive index (metals and chiral matter) or total internal reflection. Indeed, total internal reflection from air bubbles in water is one relevant source of EP light in nature [27].

After the incident wave hits the interface of a gyrotropic medium, the reflected wave becomes elliptically polarized, whose polarization characteristic angles (rotation and ellipticity) describe the Kerr rotation [28–30]. In usual scenarios, this rotation happens when the gyration vector depends on the magnetic field, leading to the well-known magneto-optic Kerr effect (MOKE) [31], which is a tool to characterize optical properties of matter systems.

The Kerr rotation has been employed as a useful tool to investigate Weyl semimetals [32, 33, 66], where the axion term yields novel effects, as frequency-dependent Kerr rotation and ellipticity angles [35]. These effects can be used to design optical devices, such as chiral filters, circular polarizers or optical isolators, since it is possible to prevent the transmission of RCP and LCP waves at certain frequency ranges [36, 37]. In thin-film topological insulators, a giant Kerr rotation of $\pi/2$ in the quantized limit has been predicted to occur [38] at a low-frequency regime. The magnitude of Kerr rotations is quite small,

* pedro.dss@ufma.br; pdiegoss.10@gmail.com

† ronald123.araujo@gmail.com

‡ manojr.ufma@gmail.com

being less than 1 degree in usual materials [39] and of the order 10^{-6} to 10^{-4} rad in topological insulators [40]. The evaluation of the Kerr rotation has been magenta used as a relevant tool to probe different materials, high-precision measurement in quantum systems [41], unconventional superconductors [42], and media modeled by CPT-even and Lorentz symmetry violating electrodynamics [43].

Another scenario studied in the last few years is dielectric matter supporting magnetic currents, in connection with the chiral magnetic effect (CME). Such an effect consists of a macroscopic magnetic current law, $\mathbf{J} = \sigma^B \mathbf{B}$, originated from the asymmetry between the number density of left- and right-handed chiral fermions [44, 45]. The CME has been investigated in several distinct situations [46–51], including Weyl semimetals (WSMs) [52–54]. Propagation of electromagnetic waves in a dispersive dielectric endowed with magnetic conductivity, assumed as an intrinsic property of the medium on equal footing to the permittivity, was also scrutinized revealing unusual features [56–58].

The vast scenario of research on the relevance of electromagnetic properties for optical material characterization, as well as recent developments in the electrodynamics of dielectrics bearing magnetic currents (in connection with WSMs), is a strong motivation for investigating the optical reflection properties in an axion coupling dielectric surface. In this sense, the present work is devoted to analyzing the optical reflection aspects in an interface between a usual dielectric and a dielectric endowed with magnetic current, $\mathbf{J} = \sigma^B \mathbf{B}$, where σ^B is the magnetic conductivity.

This paper is outlined as follows. In Sec. II, we briefly review the basic aspects of dielectric media endowed with magnetic current. In Sec. III, we derive the reflection coefficients considering incident wave with s - and p -polarizations, examining the exotic frequency dependence on the total reflection. In Sec. IV, we address the critical angles for null reflection that lead to the determination of the Brewster angles. In Sec. V, other optical properties, such as Goos-Hänchen effect and complex Kerr rotation, are discussed. Finally, we summarize our results and prospects in Sec. VI.

II. CHIRAL DIELECTRIC ENDOWED WITH MAGNETIC CONDUCTIVITY

Classical electromagnetic and optical properties of a dielectric medium in the presence of a magnetic current density have been recently addressed [56–58]. In this section, we briefly review the main aspects, taking as a starting point the Maxwell equations,

$$\nabla \cdot \mathbf{D} = 0, \quad \nabla \times \mathbf{E} + \frac{\partial \mathbf{B}}{\partial t} = \mathbf{0}, \quad (1a)$$

$$\nabla \cdot \mathbf{B} = 0, \quad \nabla \times \mathbf{H} - \frac{\partial \mathbf{D}}{\partial t} = \mathbf{J}, \quad (1b)$$

where \mathbf{J} is the current density. The system is ruled by conventional constitutive relations,

$$\mathbf{D} = \epsilon \mathbf{E}, \quad \mathbf{B} = \mu \mathbf{H}, \quad (2)$$

where ϵ is the electric permittivity and μ is the magnetic permeability. The magnetic current constitutive relation can be written in terms of the conductivity tensor, σ_{ij}^B ,

$$J^i = \sigma_{ij}^B B^j \quad (3)$$

which replaced in Maxwell's equations, in the plane-wave *ansatz*, yields

$$(\mathbf{k} \times \mathbf{k} \times \mathbf{E})^i + \mu \epsilon \omega^2 E^i + i \mu \sigma_{ij}^B (\mathbf{k} \times \mathbf{E})^j = 0. \quad (4)$$

The wave equation for the electric field amplitude is

$$[\mathbf{k}^2 \delta_{ij} - k_i k_j - \omega^2 \mu \bar{\epsilon}_{ij}(\omega)] E^j = 0, \quad (5)$$

with the effective permittivity tensor

$$\bar{\epsilon}_{ij}(\omega) = \epsilon(\omega) \delta_{ij} - \frac{i}{\omega^2} \sigma_{ia}^B \epsilon_{abj} k_b. \quad (6)$$

For an isotropic magnetic conductivity, $\sigma_{ij}^B = \Sigma \delta_{ij}$, where Σ is a real parameter, one obtains a Hermitian permittivity,

$$\bar{\epsilon}_{ij}(\omega) = \epsilon \delta_{ij} + \frac{i\Sigma}{\omega^2} \epsilon_{ijb} k_b, \quad (7)$$

which assures energy conservation and the absence of dissipation. Relation (5) may also be written as

$$M_{ij} E^j = 0, \quad (8)$$

with

$$M_{ij} = \mathbf{k}^2 \delta_{ij} - k_i k_j - \omega^2 \mu \bar{\epsilon}_{ij}(\omega). \quad (9)$$

The dispersion relations of the model are the non-trivial solutions of Eq. (8), obtained requiring $\det[M_{ij}] = 0$, which provides distinct real refractive indices,

$$n_{\pm} = \sqrt{\mu\epsilon + \left(\frac{\mu\Sigma}{2\omega}\right)^2} \pm \frac{\mu\Sigma}{2\omega}. \quad (10)$$

These indices were first carried out in Refs. [56, 57], defining a dispersive non-absorbing medium endowed with birefringence. The propagation modes for the indices (10), obtained from the relation $M_{ij} E_j = 0$, are

$$\mathbf{E}_{\pm} = \frac{1}{n\sqrt{2(n_1^2 + n_3^2)}} \begin{pmatrix} nn_3 \mp in_1 n_2 \\ \pm i(n_1^2 + n_3^2) \\ \mp in_2 n_3 - nn_1 \end{pmatrix}, \quad (11)$$

which for a wave propagating at the Z -axis, $\mathbf{n} = (0, 0, n_3)$, yields

$$\mathbf{E}_{\pm} = \frac{1}{\sqrt{2}} \begin{pmatrix} 1 \\ \pm i \\ 0 \end{pmatrix}. \quad (12)$$

The circular birefringence is quantified by the specific rotatory power δ [59–61],

$$\delta = -\frac{\omega}{2}[\text{Re}(n_+) - \text{Re}(n_-)], \quad (13)$$

which measures the rotation of the oscillation plane of linearly polarized light per unit traversed length in the medium, with n_+ and n_- associated with left and right-handed circularly polarized waves, respectively. For the refractive indices (10), the rotatory power is

$$\delta = -\frac{\mu\Sigma}{2}. \quad (14)$$

There exists a relevant interplay between the CME and the Maxwell-Carroll-Field-Jackiw (MCFJ) electrodynamics [62, 63], which contains non-dynamical axion terms. In fact, the magnetic current term appears in the axion Lagrangian [64–68],

$$\mathcal{L} = -\frac{1}{4}F^{\mu\nu}F_{\mu\nu} + \theta(\mathbf{E} \cdot \mathbf{B}), \quad (15)$$

where the axion field θ modifies the non-homogeneous Maxwell equations with derivative terms,

$$\nabla \cdot \mathbf{E} = \rho - \nabla\theta \cdot \mathbf{B}, \quad (16)$$

$$\nabla \times \mathbf{B} - \partial_t \mathbf{E} = \mathbf{j} + (\partial_t \theta)\mathbf{B} + \nabla\theta \times \mathbf{E}. \quad (17)$$

The axion gradient composes the anomalous charge density term, $\nabla\theta \cdot \mathbf{B}$, and the anomalous Hall current, $\nabla\theta \times \mathbf{B}$. On the other hand, the time derivative, $(\partial_t \theta)\mathbf{B}$, plays the role of the chiral magnetic current [68]. For a cold axion dark matter, $\nabla\theta = \mathbf{0}$, equations (16) and (17) read

$$\nabla \cdot \mathbf{E} = \rho, \quad \nabla \times \mathbf{B} - \partial_t \mathbf{E} = \mathbf{j} + (\partial_t \theta)\mathbf{B}, \quad (18)$$

with $(\partial_t \theta)$ standing in the place of the chiral magnetic conductivity. The connection between CME and axion electrodynamics finds applications in Weyl semimetals [69–71] and Casimir effect [72]. Nonlocal extensions of axion electrodynamics were implemented in extended constitutive relations to investigate optical properties of exotic metamaterials [73].

III. REFLECTION AT THE INTERFACE BETWEEN ORDINARY DIELECTRIC AND DIELECTRIC ENDOWED WITH MAGNETIC CONDUCTIVITY

Let us consider a scenario of reflection of the electromagnetic wave at the interface between two media: a conventional dielectric (μ_1, ϵ_1), and a dielectric endowed with magnetic conductivity ($\mu_2, \epsilon_2, \sigma^B$). More specifically, we consider the case where the medium 2 has isotropic magnetic conductivity, $\sigma_{ij}^B = \Sigma \delta_{ij}$, for which the refractive index of the medium 2 is given by Eq. (10), that is,

$$n_{2\pm} = \sqrt{\mu_2 \epsilon_2 + \left(\frac{\mu_2 \Sigma}{2\omega}\right)^2} \pm \frac{\mu_2 \Sigma}{2\omega}, \quad (19)$$

as discussed in Sec. II. Assuming that both media are governed by conventional constitutive relations as the ones of Eq. (2) and taking the usual boundary conditions for the electromagnetic field in the medium with magnetic conductivity, the reflection equations for the fields of Fig. 1 read

$$E_{\perp}^R = r_{\perp} E_{\perp}, \quad (20)$$

$$E_{\parallel}^R = r_{\parallel} E_{\parallel}, \quad (21)$$

where the Fresnel coefficients are

$$r_s = r_{\perp} = \frac{n_1 \mu_2 \cos \theta_1 - n_2 \mu_1 \cos \theta_2}{n_1 \mu_2 \cos \theta_1 + n_2 \mu_1 \cos \theta_2}, \quad (22)$$

$$r_p = r_{\parallel} = \frac{n_2 \mu_1 \cos \theta_1 - n_1 \mu_2 \cos \theta_2}{n_2 \mu_1 \cos \theta_1 + n_1 \mu_2 \cos \theta_2}. \quad (23)$$

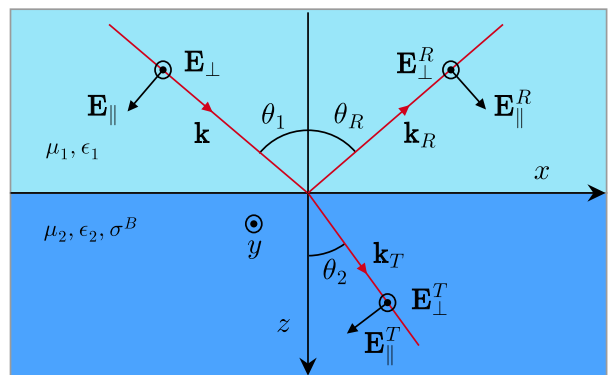


FIG. 1. Interface between a usual and a chiral dielectric. Electric field components of the incident, reflected, and transmitted waves.

Taking into account that medium 2 presents two different refractive indices, see n_{2+} and n_{2-} of Eq. (19), each mode travels with different phase velocities and there occurs two refracted (or transmitted) waves [3], each one associated with one propagating mode. This is a manifestation of birefringence, a feature of optical active media.

Considering $n_1 = \sqrt{\mu_1 \epsilon_1}$ and the indices (19), the Fresnel coefficients for polarization-s and polarization-p are

$$r_{\perp}^{\pm} = \frac{f_{\theta_1} - \mu_1 \sqrt{\mu_2 \epsilon_2 + \left(\frac{\mu_2 \Sigma}{2\omega}\right)^2} \cos \theta_2 \mp \frac{\mu_2 \Sigma}{2\omega} \mu_1 \cos \theta_2}{f_{\theta_1} + \mu_1 \sqrt{\mu_2 \epsilon_2 + \left(\frac{\mu_2 \Sigma}{2\omega}\right)^2} \cos \theta_2 \pm \frac{\mu_2 \Sigma}{2\omega} \mu_1 \cos \theta_2}, \quad (24)$$

$$r_{\parallel}^{\pm} = \frac{\mu_1 \sqrt{\mu_2 \epsilon_2 + \left(\frac{\mu_2 \Sigma}{2\omega}\right)^2} \cos \theta_1 \pm \frac{\mu_2 \Sigma}{2\omega} \mu_1 \cos \theta_1 - f_{\theta_2}}{\mu_1 \sqrt{\mu_2 \epsilon_2 + \left(\frac{\mu_2 \Sigma}{2\omega}\right)^2} \cos \theta_1 \pm \frac{\mu_2 \Sigma}{2\omega} \mu_1 \cos \theta_1 + f_{\theta_2}}, \quad (25)$$

with

$$f_{\theta_{1,2}} = \mu_2 \sqrt{\mu_1 \epsilon_1} \cos \theta_{1,2}. \quad (26)$$

Given the coefficients (24) and (25), one can write the reflection coefficient R (or reflectance) as follows [1]:

$$R_{\perp}^{\pm} = |r_{\perp}^{\pm}|^2, \quad (27)$$

$$R_{\parallel}^{\pm} = |r_{\parallel}^{\pm}|^2. \quad (28)$$

Unlike the usual dielectric scenario (where $\Sigma = 0$), the R coefficients (27) and (28) depend on the frequency of the incident electromagnetic wave, ω , and on the incidence and refraction angles. This kind of dependence appears typically in interfaces separating an ordinary dielectric and a conducting medium. The coefficients (27) and (28) can be rewritten in terms of the transmission angle θ_2 by using the Snell law, $n_1 \sin \theta_1 = n_{2\pm} \sin \theta_{2\pm}$, implying

$$\theta_{2\pm} = \arcsin \left[\frac{\sqrt{\mu_1 \epsilon_1} \sin \theta_1}{\sqrt{\mu_2 \epsilon_2 + \left(\frac{\mu_2 \Sigma}{2\omega}\right)^2 \pm \frac{\mu_2 \Sigma}{2\omega}}} \right]. \quad (29)$$

The latter expressions are obtained assuming that both modes obey Snell's law [3, 74]. This scenario also happens for both ordinary and extraordinary rays in anisotropic materials when incident light impinges the interface perpendicularly to the optical axis [75, 76].

To get more physical insights about the influence of Σ on R_{\perp}^{\pm} and R_{\parallel}^{\pm} , we will plot them in terms of frequency for $\theta_1(\text{rad}) = \{0, \frac{\pi}{6}, \frac{\pi}{4}, \frac{\pi}{3}, \frac{5\pi}{12}\}$.

A. Incident wave with s -polarization

For the incident wave in s -polarization, the reflection coefficient is given by the two possibilities, R_{\perp}^{\pm} , given in Eq. (27). We begin analyzing the behavior of the coefficient R_{\perp}^+ , whose magnitude decreases with the frequency, as depicted in Fig. 2.

As shown, the asymptotic value of R_{\perp}^+ (defined for very large frequencies) diminishes with the incidence angle. In true, this happens equally for the asymptotic value of R_{\perp}^- , since the expressions (24) and (27) yield the same result in the high-frequency limit, namely

$$R_{\perp}^{\pm} \simeq \left| \frac{\mu_2 \sqrt{\mu_1 \epsilon_1} \cos \theta_1 - \mu_1 \sqrt{\mu_2 \epsilon_2} \cos \theta_{2+}}{\mu_2 \sqrt{\mu_1 \epsilon_1} \cos \theta_1 + \mu_1 \sqrt{\mu_2 \epsilon_2} \cos \theta_{2+}} \right|^2, \quad (30)$$

or

$$R_{\perp}^{\pm} \simeq \left| \frac{\mu_2 \sqrt{\mu_1 \epsilon_1} \cos \theta_1 - \mu_1 \sqrt{\mu_2 \epsilon_2} \sqrt{1 - \frac{\mu_1 \epsilon_1}{\mu_2 \epsilon_2} \sin^2 \theta_1}}{\mu_2 \sqrt{\mu_1 \epsilon_1} \cos \theta_1 + \mu_1 \sqrt{\mu_2 \epsilon_2} \sqrt{1 - \frac{\mu_1 \epsilon_1}{\mu_2 \epsilon_2} \sin^2 \theta_1}} \right|^2. \quad (31)$$

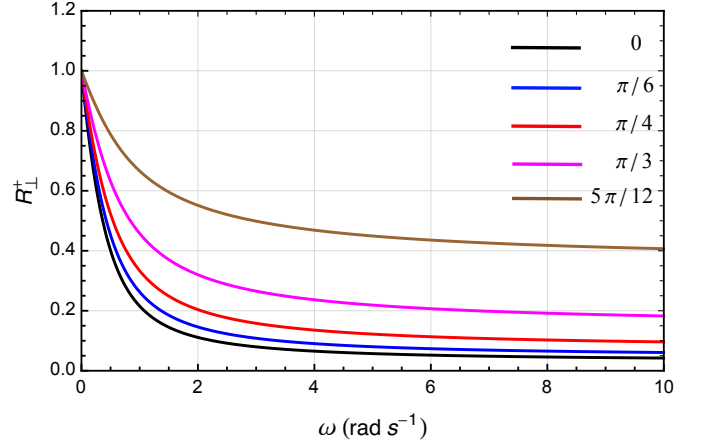


FIG. 2. Reflection coefficient R_{\perp}^+ in terms of frequency ω for fixed incidence angles. For the medium 1, we have used $\mu_1 = 1$, $\epsilon_1 = 1$, while for the medium 2: $\mu_2 = 1$, $\epsilon_2 = 2$, $\Sigma = 2 \text{ s}^{-1}$.

The asymptotic expression (31) reveals that the effect of the magnetic conductivity is suppressed in the high-frequency limit, indicating that R_{\perp}^{\pm} recover the reflection coefficient usual case (obtained for dielectric with $\Sigma = 0$). This feature is properly illustrated in Fig. 3 for some parameter values.

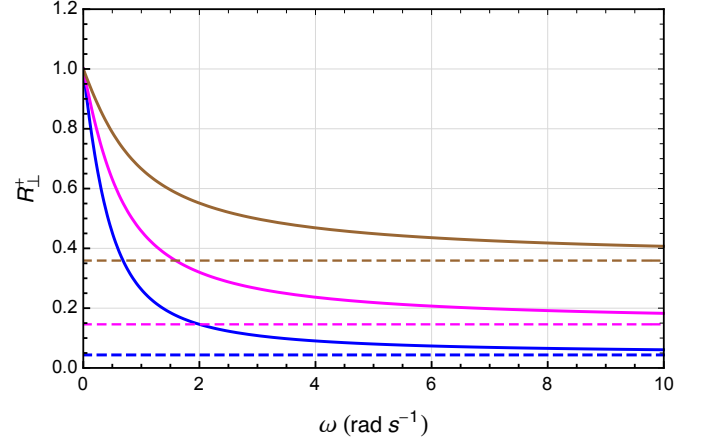


FIG. 3. Reflection coefficient R_{\perp}^+ in terms of frequency ω for fixed incidence angles $\theta_1 = \pi/6$ (blue), $\theta_1 = \pi/3$ (magenta), and $\theta_1 = 5\pi/12$ (brown). For the medium 1, we have used $\mu_1 = 1$, $\epsilon_1 = 1$, and for the medium 2: $\mu_2 = 1$, $\epsilon_2 = 2$, $\Sigma = 2 \text{ s}^{-1}$ (solid curves), and $\Sigma = 0$ (dashed lines).

The dependence of R_{\perp}^+ on the incidence angle θ_1 is depicted in Fig. 4. We observe that by increasing the value of Σ (in terms of Σ/ω), the R_{\perp}^+ curve moves away from the standard scenario (dashed black line), enhancing the magnitude of the reflection coefficient.

As for the reflection coefficient R_{\perp}^- , its behavior in terms of frequency differs appreciably from the one of R_{\perp}^+ , as shown in Fig. 5. For a non-null Σ and general incidence angles (excluding normal incidence), the reflec-

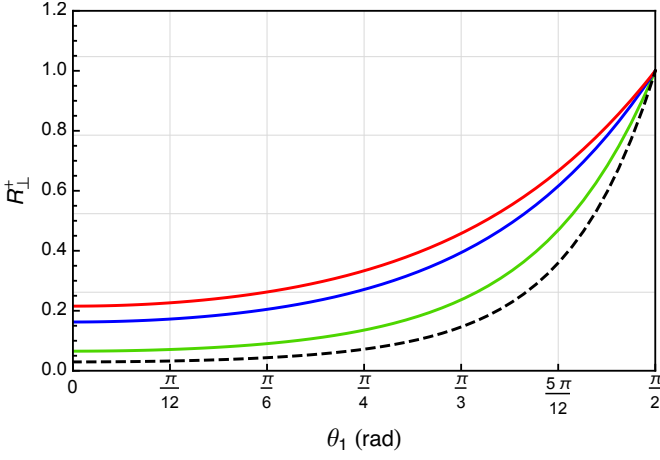


FIG. 4. Reflection coefficient R_{\perp}^{+} in terms of the incidence angle θ_1 . For the medium 1, we have used $\mu_1 = 1$, $\epsilon_1 = 1$, and for the medium 2: $\mu_2 = 1$, $\epsilon_2 = 2$, $\Sigma/\omega = 0.5$ (green), $\Sigma/\omega = 1.5$ (blue), and $\Sigma/\omega = 2$ (red). The dashed black line represents the usual case ($\Sigma = 0$).

tion coefficient becomes equal to 1 in the low-frequency region defined by $0 < \omega \leq \omega_i$, where ω_i is given by

$$\omega_i = \frac{\mu_2 \Sigma \sqrt{\mu_1 \epsilon_1} |\sin \theta_1|}{|\mu_2 \epsilon_2 - \mu_1 \epsilon_1 \sin^2 \theta_1|}. \quad (32)$$

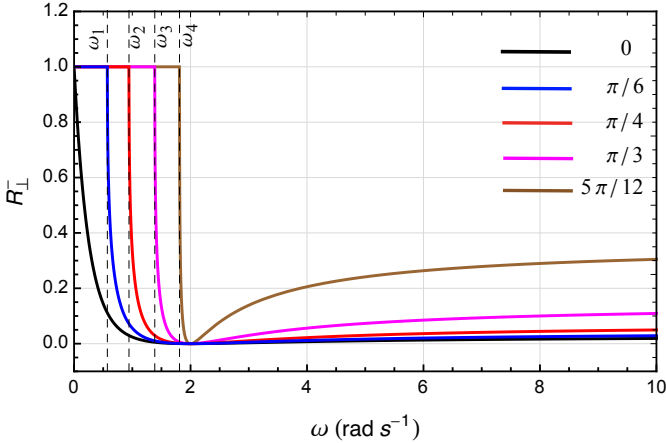


FIG. 5. Reflection coefficient R_{\perp}^{-} in terms of frequency ω for fixed incidence angles. For the medium 1 we have used $\mu_1 = 1$, $\epsilon_1 = 1$, and for the medium 2: $\mu_2 = 1$, $\epsilon_2 = 2$, $\Sigma = 2 \text{ s}^{-1}$. The vertical dashed lines indicate the frequencies ω_i of Eq. (32) which define the limit of the total reflection window (for each case).

The behavior $R_{\perp}^{-} = 1$ in the window $0 < \omega \leq \omega_i$ represents a scenario of total reflection induced by the non-null magnetic conductivity, Σ . Indeed, in such a region the refractive index n_{2-} becomes less than n_1 , so Snell's law yields total reflection. This low-frequency effect does not happen in the usual scenario of an ordinary dielectric - ordinary dielectric interface, whose non-dispersive

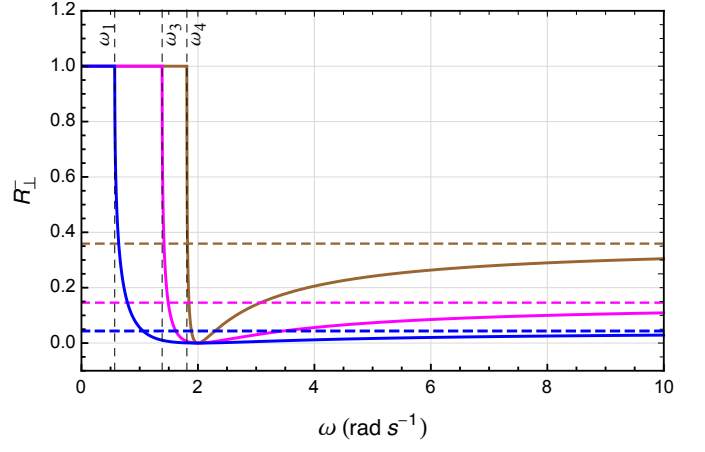


FIG. 6. Reflection coefficient R_{\perp}^{-} in terms of frequency ω for fixed incidence angles $\theta_1 = \pi/6$ (blue), $\theta_1 = \pi/3$ (magenta), and $\theta_1 = 5\pi/12$ (brown). For the medium 1, we have used $\mu_1 = 1$, $\epsilon_1 = 1$, while for the medium 2: $\mu_2 = 1$, $\epsilon_2 = 2$, $\Sigma = 2 \text{ s}^{-1}$ (solid curves), and $\Sigma = 0$ (dashed lines).

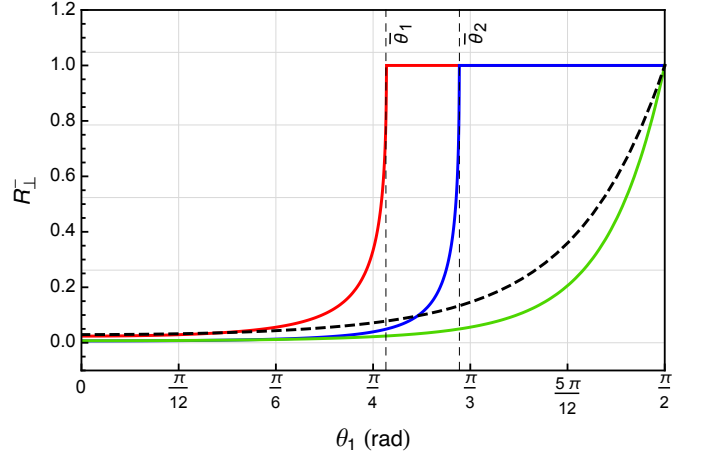


FIG. 7. Reflection coefficient R_{\perp}^{-} in terms of the incidence angle θ_1 . For the medium 1, we have used $\mu_1 = 1$, $\epsilon_1 = 1$, and for the medium 2: $\mu_2 = 1$, $\epsilon_2 = 2$, $\Sigma/\omega = 0.5$ (green line), $\Sigma/\omega = 1.5$ (blue line), and $\Sigma/\omega = 2$ (red). The dashed black line represents the usual case ($\Sigma = 0$). The vertical dashed lines indicate $\bar{\theta}_1 \simeq 0.261 \pi$ rad and $\bar{\theta}_2 \simeq 0.324 \pi$ rad, accordingly to Eq. (34).

behavior is represented by the horizontal lines in Fig. 6. Besides this first peculiar aspect, the coefficient displays another interesting feature. It becomes null, $R_{\perp}^{-} = 0$, for a specific value of frequency, ω_0 , given by

$$\omega_0 = \frac{\mu_2 \Sigma \sqrt{\mu_1 \epsilon_1} \sqrt{\mu_1^2 \sin^2 \theta_1 + \mu_2^2 \cos^2 \theta_1}}{|\mu_1 \mu_2 \epsilon_2 - \epsilon_1 (\mu_1^2 \sin^2 \theta_1 + \mu_2^2 \cos^2 \theta_1)|}, \quad (33)$$

being also a consequence of non-null magnetic conductivity. For all examples in Fig. 5, one finds $R_{\perp}^{-} = 0$ for $\omega = 2 \text{ rad s}^{-1}$.

On the other hand, the general behavior of R_{\perp}^{-} in terms of the incidence angle θ_1 is displayed in Fig. 7, where one

observes another peculiar property, given in terms of the regions fulfilling total reflection, that is, $R_{\perp}^{-} = 1$. These regions occur for $\Sigma/\omega > 1$ (low-frequency regime), being defined for $\bar{\theta}_i < \theta_1 < \pi/2$, where

$$\bar{\theta}_i^{\pm} = \arcsin \left[\frac{1}{\sqrt{\mu_1 \epsilon_1}} \left(\sqrt{\mu_2 \epsilon_2 + \frac{\mu_2^2 \Sigma^2}{4\omega^2}} - \frac{\mu_2 \Sigma}{2\omega} \right) \right]. \quad (34)$$

For $\Sigma/\omega < 1$, the value of $\bar{\theta}_i$ becomes complex, meaning that the flat horizontal region, $R_{\perp}^{-} = 1$, does not occur in the high-frequency limit or very low Σ , which includes the scenario of a conventional dielectric, $\Sigma = 0$ (see the dashed black line in Fig. 7).

B. Incident wave with p -polarization

For incident wave with p -polarization, the reflection coefficient is R_{\parallel}^{\pm} of Eq. (28). Figures 8 and 9 depict the reflectance R_{\parallel}^{+} and R_{\parallel}^{-} , respectively, in terms of the frequency. The profile of R_{\parallel}^{+} may exhibit a frequency value for null reflection, which does not occur for R_{\perp}^{+} (see Fig. 3). Figure 9 should be compared with Fig. 5, revealing nearly the same qualitative behavior for R_{\parallel}^{-} and R_{\perp}^{-} .

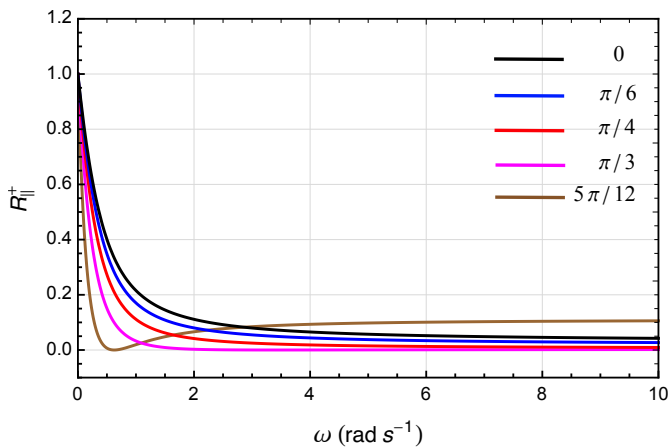


FIG. 8. Reflection coefficient R_{\parallel}^{+} in terms of frequency ω for fixed incidence angles. For the medium 1, we have used $\mu_1 = 1$, $\epsilon_1 = 1$, and for the medium 2: $\mu_2 = 1$, $\epsilon_2 = 2$, $\Sigma = 2 \text{ s}^{-1}$.

We point out that $R_{\parallel}^{\pm} = 0$ can occur for specific frequency values, which are determined by the real and positive solutions of

$$\omega \left(\mu_1 \epsilon_2 - \mu_2 \epsilon_1 \frac{\cos^2 \theta_{2\pm}}{\cos^2 \theta_1} \right) \pm \mu_2 \Sigma \sqrt{\mu_1 \epsilon_1} \frac{\cos \theta_{2\pm}}{\cos \theta_1} = 0, \quad (35)$$

with $\theta_{2\pm}$ given by Eq. (29) and the upper and lower signs providing the solutions for $R_{\parallel}^{+} = 0$ and $R_{\parallel}^{-} = 0$, respectively.

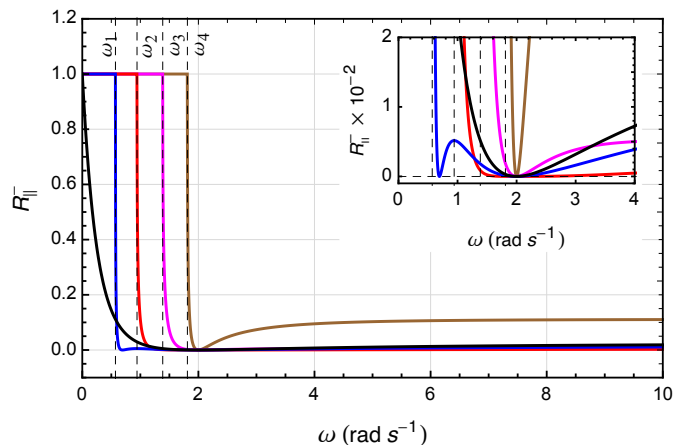


FIG. 9. Reflection coefficient R_{\parallel}^{-} in terms of frequency ω for fixed incidence angles (radians): 0 (black), $\pi/6$ (blue), $\pi/4$ (red), $\pi/3$ (magenta), and $5\pi/12$ (brown). Here, we have used $\mu_1 = \mu_2 = 1$, $\epsilon_1 = 1$, $\epsilon_2 = 2$ e $\Sigma = 2 \text{ s}^{-1}$. The inset plot highlights the behavior of R_{\parallel}^{-} around its roots and shows that R_{\parallel}^{-} has two roots in ω for $\theta_1 = \pi/6$, differing from all the other θ_1 cases, where only one root (in $\omega = 2 \text{ rad s}^{-1}$) is found.

The behavior of R_{\parallel}^{\pm} with the incidence angle is illustrated in Figs. 10 and 11, respectively. Both are different from the coefficients R_{\perp}^{+} of Fig. 4 and R_{\perp}^{-} of Fig. 7. As shown in Fig. 10, the coefficient R_{\parallel}^{+} initially decreases with θ_1 , reaching a null value at the Brewster angle, and after increasing to the maximum value ($R_{\parallel}^{+} = 1$) while the angle θ_1 approaches $\pi/2$. This behavior differs from the R_{\perp}^{+} profile, which grows up monotonically (see Fig. 4).

As for the behavior of R_{\parallel}^{-} with θ_1 , given in Fig. 11, there is a near similarity with the profile of R_{\perp}^{-} of Fig. 7, both presenting a window of total reflection starting in a given value of incidence angle, $\bar{\theta}_i$, given by

$$\bar{\theta}_i^{\parallel} = \arcsin \left[\frac{1}{\sqrt{\mu_1 \epsilon_1}} \left(\sqrt{\mu_2 \epsilon_2 + \frac{\mu_2^2 \Sigma^2}{4\omega^2}} - \frac{\mu_2 \Sigma}{2\omega} \right) \right]. \quad (36)$$

The distinction between them rests in the slightly decreasing magnitude observed before reaching the Brewster angle.

C. Total reflection

In the last section, the total reflection was reported for $R_{\perp, \parallel}^{-} = 1$ in the frequency window $0 < \omega < \omega_i$, with ω_i of Eq. (32). The total reflection also happens when the incidence angle is defined in the range $\theta_i < \theta_1 < \pi/2$, with $\bar{\theta}_i$ of Eq. (34) and Eq. (36), respectively, also

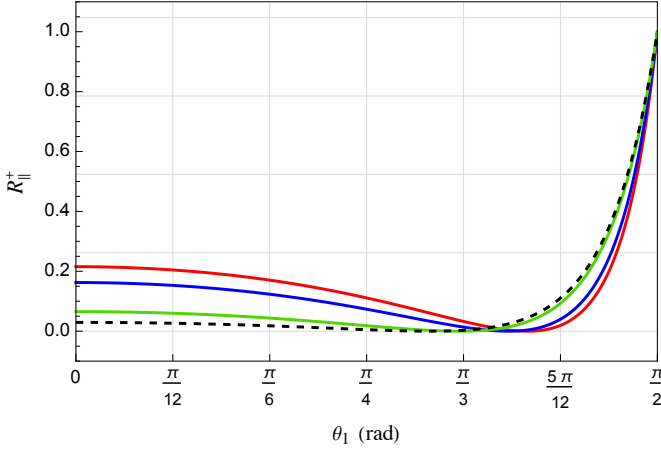


FIG. 10. Reflection coefficient R_{\parallel}^+ in terms of the incidence angle θ_1 . Medium 1 defined by $\mu_1 = 1$, $\epsilon_1 = 1$, and medium 2 by $\mu_2 = 1$, $\epsilon_2 = 2$, $\Sigma/\omega = 0.5$ (green), $\Sigma/\omega = 1.5$ (blue), and $\Sigma/\omega = 2$ (red). The dashed black line represents the usual case ($\Sigma = 0$).

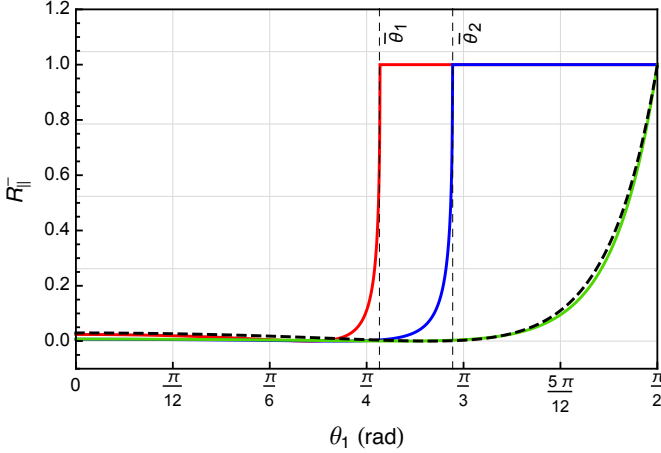


FIG. 11. Reflection coefficient R_{\parallel}^- in terms of the incidence angle θ_1 . For the medium 1, we have used $\mu_1 = 1$, $\epsilon_1 = 1$, and for the medium 2: $\mu_2 = 1$, $\epsilon_2 = 2$, $\Sigma/\omega = 0.5$ (black), $\Sigma/\omega = 1.5$ (blue), and $\Sigma/\omega = 2$ (red). The dashed black line represents the usual case ($\Sigma = 0$). The vertical dashed lines indicate $\bar{\theta}_1 \simeq 0.261 \pi$ rad and $\bar{\theta}_2 \simeq 0.324 \pi$ rad, accordingly to Eq. (36).

written as

$$\bar{\theta}_i^{\pm} = \arcsin \left[\frac{1}{\sqrt{\mu_1 \epsilon_1}} \left(\sqrt{\mu_2 \epsilon_2 + \frac{\mu_2^2 \Sigma^2}{4\omega^2}} \pm \frac{\mu_2 \Sigma}{2\omega} \right) \right]. \quad (37)$$

Due to the values of the constitutive parameters adopted in the plots of the latter section, $\mu_2 \epsilon_2 > \mu_1 \epsilon_1$, the total reflection was verified only for R_{\parallel}^- and R_{\perp}^- . However, such a phenomenon can also occur for the polarization mode + if we adopt the condition $\mu_2 \epsilon_2 < \mu_1 \epsilon_1$, as shown in the first line of Table I. The situations of total

reflection of Fig. 9 are contained in the conditions of the second row and second column of Tab. I.

TABLE I. Conditions for total reflection.

$R_{\perp, \parallel}^+ = 1$	$R_{\perp, \parallel}^- = 1$
$\mu_2 \epsilon_2 < \mu_1 \epsilon_1,$	$\mu_2 \epsilon_2 \leq \mu_1 \epsilon_1,$
$\omega > \frac{\mu_2 \sin \theta_1 \Sigma \sqrt{\mu_1 \epsilon_1}}{ \mu_1 \epsilon_1 \sin^2 \theta_1 - \mu_2 \epsilon_2 }.$	$\omega > 0.$
$\mu_2 \epsilon_2 > \mu_1 \epsilon_1,$ no range in ω for it.	$\mu_2 \epsilon_2 > \mu_1 \epsilon_1,$ $0 < \omega \leq \frac{\mu_2 \sin \theta_1 \Sigma \sqrt{\mu_1 \epsilon_1}}{ \mu_2 \epsilon_2 - \mu_1 \epsilon_1 \sin^2 \theta_1 }.$
$\mu_1 = \mu_2, \epsilon_1 = \epsilon_2,$ $\Sigma < 0, \omega > 0.$	$\mu_1 = \mu_2, \epsilon_1 = \epsilon_2,$ no range in ω for it.

Table 1 also contains a special and interesting possibility of total reflection for $\epsilon_1 = \epsilon_2$ and $\mu_1 = \mu_2$. But in this case, the total reflection can only occur when $\Sigma < 0$ for $R_{\parallel, \perp}^+ = 1$ (for any value of frequency), while $R_{\perp, \parallel}^- = 1$ does not happen under these conditions. This theoretical possibility will not be discussed in this work, but it may motivate additional investigations in the future.

IV. CRITICAL ANGLES FOR NULL REFLECTION AND POLARIZATION CHANGE

In this section, we analyze the critical angles that determine the incidence configuration at which the reflection becomes null. Since we have obtained two reflection coefficients for each scenario regarding the polarizations (*s* or *p*) of the incident wave, there will be two distinct critical angles, one for each mode.

A. Critical angles for incident *s*-polarization wave

Starting from the coefficient (24), the condition for a real non-null critical angles $\theta_{1\pm}^c$, for which $R_{\perp}^{\pm} = 0$, is given by

$$\tan^2(\theta_s^c)_{\pm} = \frac{\mu_2^2 n_1^2 / \mu_1^2 - n_{2\pm}^2}{(n_{2\pm}^2 - n_1^2)}, \quad (38)$$

which also is expressed as

$$\tan^2 \theta_{s\pm}^c = \frac{\frac{\mu_2^2 \epsilon_1}{\mu_1} - \left(\sqrt{\mu_2 \epsilon_2 + \left(\frac{\mu_2 \Sigma}{2\omega} \right)^2} \pm \frac{\mu_2 \Sigma}{2\omega} \right)^2}{\left(\sqrt{\mu_2 \epsilon_2 + \left(\frac{\mu_2 \Sigma}{2\omega} \right)^2} \pm \frac{\mu_2 \Sigma}{2\omega} \right)^2 - \mu_1 \epsilon_1}. \quad (39)$$

In general, these angles constitute partial Brewster angles, since they state the incidence condition that turns null one of the two s -modes. However, if exists one frequency value for which both angles become equal, such a frequency defines a total Brewster angle for s polarization).

Considering that the constitutive parameters $(\epsilon_{1,2}, \mu_{1,2}, \Sigma)$ are real and positive, the general conditions to determine the critical angles are given in Tables II and IV of Appendix A. We observe in $c)$ row of these tables that $R_{\perp}^{+} = 0$ and $R_{\perp}^{-} = 0$ can occur simultaneously for the same set of conditions¹. However, the corresponding critical angles, θ_{s+}^c and θ_{s-}^c , are distinct, since they are defined by different expressions, see the \pm sign in Eq. (39). Consequently, one has a specific critical angle at which $R_{\perp}^{+} = 0$, $R_{\perp}^{-} \neq 0$ and another angle for $R_{\perp}^{-} = 0$, $R_{\perp}^{+} \neq 0$. To illustrate the behavior of the critical angles, Figure 12 shows the critical angles, θ_{s+}^c and θ_{s-}^c , in terms of the dimensionless parameter $y = \omega/\Sigma$, for the conditions given in row $d)$ of tables II and IV.

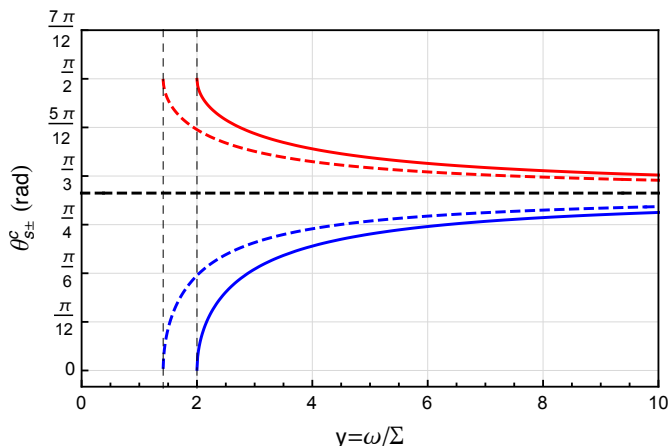


FIG. 12. Critical angles θ_{1+}^c (azul) and θ_{1-}^c (red) in terms of frequency $y = \omega/\Sigma$. The solid curves indicate the critical angles when the medium 1 is described by $\mu_1 = 1$, $\epsilon_1 = 1$, and the medium 2 by $\mu_2 = 2$, $\epsilon_2 = 1$. For the color-dashed lines, one has $\mu_1 = 1$, $\epsilon_1 = 2$ and $\mu_2 = 2$, $\epsilon_2 = 2$. The dashed black horizontal line indicates the usual case ($\Sigma = 0$). The dashed vertical lines define the lower limit for y , given by Eq. (40).

In Fig. 12, the dashed vertical lines indicate the lower bound for frequency ω , i. e., they stipulate the window $y > \hat{y}$ in which the critical angles can exist, with \hat{y} given by

$$\hat{y} = \sqrt{\frac{\mu_1}{\epsilon_1} \frac{\mu_2}{\mu_2 - \mu_1}}, \quad (40)$$

¹ If one chooses another set condition from Tab. III (or V) of Appendix A, for instance, one would obtain only a critical angle for $R_{\perp}^{+} = 0$ (or for $R_{\perp}^{-} = 0$), since the existence of only one critical angle would be granted. This explains the reason to have chosen the sets of row $c)$ of Tabs. II and IV, which are able to provide both $R_{\perp}^{+} = 0$ and $R_{\perp}^{-} = 0$.

and $\mu_2 > \mu_1$, since we are considering the conditions of row $c)$ of Tabs. II and IV. As the corresponding curves for θ_{s+}^c (azul) and θ_{s-}^c (red) in Fig. 12 never cross each other, there is no frequency in which $\theta_{1+}^c = \theta_{1-}^c$. The absence of a unique angle yielding simultaneously $R_{\perp}^{+} = 0$ and $R_{\perp}^{-} = 0$ avoids the definition of a total Brewster angle (for total null reflection for the s -polarization). Therefore, for the set of examined parameters, only partial s -Brewster angles were reported.

B. Circular Polarized reflected wave for s -polarization incident wave

The existence of partial Brewster angles engenders the polarization change of the reflected wave in relation to incident one. Indeed, given a linear s -polarized wave, which can be regarded as the sum of RCP and LCP waves, $E_{0s} = E_- + E_+$, respectively, the reflected ray can emerge as circularly polarized, as follows:

- For the case $\theta = \theta_{s+}^c$, the LCP wave is suppressed and the reflected wave contains only the piece E_- , becoming RCP.
- For the case $\theta = \theta_{s-}^c$, the RCP wave is suppressed and the reflected wave contains only the piece E_+ , becoming LCP.

For the special case of non-magnetic materials ($\mu_1 = \mu_2 \simeq \mu_0$), expression (38) yields $\tan^2 \theta_{1\pm}^c = -1$, which has no real solutions. Therefore, there are no critical angles for s -polarized incident wave at the interface between non-magnetic media, as it occurs in the usual dielectric reflection. This is due to the fact the expression (38) has the same structure as the usual dielectric-dielectric interface. The next section shows that this special case can occur for the incident wave p -polarized.

C. Critical angles and polarization change for p -polarization incident wave

When the incident wave is p -polarized, the coefficient (25) yields critical angles defined by

$$\tan^2 \theta_{p\pm}^c = \frac{\mu_1^2 n_{2\pm}^4 - \mu_2^2 n_1^2 n_{2\pm}^2}{\mu_2^2 n_1^2 (n_{2\pm}^2 - n_1^2)}, \quad (41)$$

with $n_1^2 = \mu_1 \epsilon_1$ and $n_{2\pm}$ given in Eq. (19). The angles (41) only occur when the constitutive parameters fulfill one of the several possible sets of conditions in Tabs. III and V for real and positive constitutive parameters.

Figure 13 depicts the critical angles $\theta_{p\pm}^c$ in terms of the dimensionless parameter $y = \omega/\Sigma$ for the conditions given in the row $c)$ of Tab. III and row $d)$ of Tab. V, whose choice allows us to represent θ_{p+}^c and θ_{p-}^c in the same graph, due to the same reason explained in the latter “ s ”-polarization section.

According to the set of conditions adopted, both the critical angles are only defined when $y < \bar{y}$, with \bar{y} given in Eq. (42). Differently from the previous s -polarized scenario, the present case allows $\theta_{p+}^c = \theta_{p-}^c$ for a certain value of y , designated as $\bar{y} = \bar{\omega}/\Sigma$, and given by

$$\bar{y} = \sqrt{\frac{\mu_1}{\epsilon_1}} \sqrt{\frac{\mu_2}{2(\mu_2 - \mu_1)}}. \quad (42)$$

Thus, by using \bar{y} , one determines the frequency $\bar{\omega}$ for which one simultaneously has $R_{\parallel}^+ = 0$ and $R_{\parallel}^- = 0$, defining a total Brewster angle, labeled as $\theta_p|_{\bar{\omega}}$, at which it also occurs polarization modification. Indeed, for the particular conditions adopted in rows c) of Tab. III and row d) of Tab. V, we observe a total Brewster angle of $\pi/4$. Furthermore, considering a mixed incident linearly polarization written as $E_0 = E_s + E_p$, the reflected ray becomes s -polarized, $E_R = E_s$. For other values of frequency, $\omega \neq \bar{\omega}$, in which only partial Brewster angles hold, there occurs a change of p -linear polarization, $E_{0p} = E_- + E_+$, to the circular one, as follows:

- For the case $\theta = \theta_{p+}^c$, the LCP wave is suppressed and the reflected wave contains only the piece E_- , becoming RCP.
- For the case $\theta = \theta_{p-}^c$, the RCP wave is suppressed and the reflected wave contains only the piece E_+ , becoming LCP.

The fact that the expression (38) has the same structure of the usual dielectric-dielectric interface implies equal results for the p -polarization, that is,

- For $\mu_1 = \mu_2$, one has $\tan \theta_{p\pm}^c = n_2/n_1$, which implies

$$\theta_{p\pm}^c + \theta_2 = \pi/2. \quad (43)$$

- For $\mu_1 > \mu_2$, one has $\tan \theta_{p\pm}^c > n_2/n_1$, which implies

$$\theta_{p\pm}^c + \theta_2 < \pi/2. \quad (44)$$

- For $\mu_1 < \mu_2$ (and $\mu_1 n_{2\pm} > \mu_2 n_1$), one has $\tan \theta_{p\pm}^c < n_2/n_1$, which yields

$$\theta_{p\pm}^c + \theta_2 > \pi/2. \quad (45)$$

V. OPTICAL EFFECTS

In this section, we discuss other relevant optical properties of the reflected wave, namely the Goos-Hänchen effect (GH) and the complex Kerr rotation angle in the reflection.

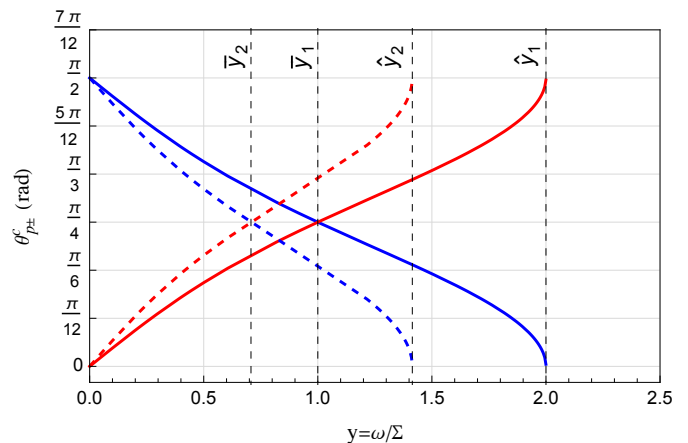


FIG. 13. Critical angles θ_{1+}^c (azul) and θ_{1-}^c (red) in terms of frequency $y = \omega/\Sigma$. Here, we have used $\mu_1 = 1$, $\mu_2 = 2$, $\epsilon_1 = \epsilon_2 = 1$ (solid curves), and $\epsilon_1 = \epsilon_2 = 2$ (dashed lines). The dashed vertical lines at $\hat{y}_{1,2}$ define the upper limit for y , according to Eq. (40). The dashed vertical lines at $\bar{y}_{1,2}$, given by Eq. (42), define the values of y where $\theta_{1+}^c = \theta_{1-}^c$. Notice that the usual scenario ($\Sigma = 0$) is not depicted since Eq. (41) has no real solutions when $\mu_2 > \mu_1$, $\epsilon_2 = \epsilon_1$ and $\Sigma = 0$.

A. Goos-Hänchen effect

When the incidence angle is greater than

$$\bar{\theta}_i^\pm = \arcsin \left[\frac{1}{\sqrt{\mu_1 \epsilon_1}} \left(\sqrt{\mu_2 \epsilon_2 + \frac{\mu_2^2 \Sigma^2}{4\omega^2}} \pm \frac{\mu_2 \Sigma}{2\omega} \right) \right], \quad (46)$$

total reflection occurs for the corresponding propagating mode. In this scenario, the associated reflected wave undergoes a lateral shift, a displacement of the reflected wave relative to the position in which there is no total reflection, given as

$$D = -\frac{\lambda}{2\pi} \frac{\partial \varphi}{\partial \theta_1}, \quad (47)$$

where λ is the wavelength of the incident light and φ is the phase acquired during total internal reflection². Such a lateral optical displacement of the reflected ray is known as the Goos-Hänchen effect [2, 5].

1. Incident wave with s -polarization

Considering the s -polarized incident wave, the reflection coefficient r_\perp^\pm of Eq. (22), in the regime of total internal reflection, can be rewritten as $r_\perp^\pm = \exp(i\varphi_s^\pm)$, with

² In a standard reflection scenario between two usual dielectrics ($\Sigma = 0$), to enable the condition for total reflection and the displacement occurrence, the incident wave travels from medium 1 to medium 2, with $n_1 > n_2$.

the phase factor

$$\varphi_s^\pm = -2 \arctan \left(\frac{\mu_1}{\mu_2} \frac{\sqrt{\sin^2 \theta_1 - \sin^2 \bar{\theta}_i^\pm}}{\cos \theta_1} \right). \quad (48)$$

The GH displacement is obtained by replacing the phase (48) in Eq. (47), providing

$$D_\perp^\pm = \frac{\lambda}{\pi} \frac{\sin \theta_1}{\sqrt{\sin^2 \theta_1 - \sin^2 \bar{\theta}_i^\pm}} g_\pm, \quad (49a)$$

$$g_\pm = \frac{\mu_1 \mu_2 \cos^2 \bar{\theta}_i^\pm}{\mu_2^2 \cos^2 \theta_1 + \mu_1^2 (\sin^2 \theta_1 - \sin^2 \bar{\theta}_i^\pm)}. \quad (49b)$$

In figure 14, we depict the lateral shift per unit length in terms of the incidence angle for magnetic and non-magnetic cases. Notice that the values of the constitutive parameters chosen here satisfy the general conditions given in the first row of the two columns of Tab. I. This explains why one can represent in the same plot both D_\perp^\pm .

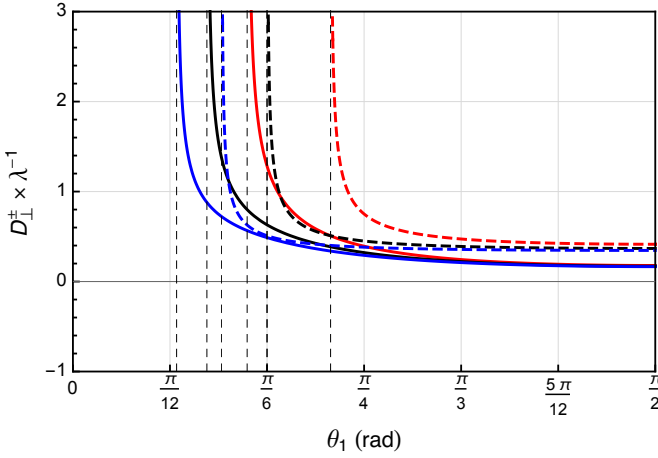


FIG. 14. The Goos-Hänchen shift D_\perp^+ (red lines) and D_\perp^- (blue lines) in terms of the incidence angle, θ_1 . The dashed lines were obtained for $\epsilon_1 = 4$, $\epsilon_2 = 1$, $\Sigma/\omega = 0.5$, $\mu_1 = 1$, $\mu_2 = 1$ and represent the GH shift for a reflection in non-magnetic media. The solid lines correspond to $\epsilon_1 = 4$, $\epsilon_2 = 1$, $\Sigma/\omega = 0.5$ and $\mu_1 = 2$, $\mu_2 = 1$, representing the GH shift for a reflection with a magnetic medium. The black lines indicate the usual case ($\Sigma = 0$). The vertical pale dashed lines indicate the critical angle above which total internal reflection occurs for each example, accordingly to Eq. (46).

For all the cases examined, the GH shift begins large for angles immediately greater than the total reflection value and decreases monotonically until reaching an asymptotical low value when the incidence angle approaches $\pi/2$. For the case the interface separates non-magnetic media, the GH asymptotic shift may be a bit larger (D_\perp^+) or smaller (D_\perp^-) than the one obtained in the usual case ($\Sigma = 0$) - see the black dashed line in Fig. 14. On the other hand, for the case where the interface

separates magnetic media ($\mu > 1$), the GH asymptotic shift is nearly equal (D_\perp^+ and D_\perp^-) to the one obtained in the usual case ($\Sigma = 0$).

So, we notice that the magnetic conductivity may alter the GH shift in reflections in non-magnetic media.

2. Incident wave with p -polarization

For incident wave p -polarized, the complex reflection coefficient is now $r_\parallel^\pm = \exp(i\varphi_p^\pm)$ where

$$\varphi_p^\pm = -2 \arctan \left(\frac{\mu_2}{\mu_1} \frac{\sqrt{\sin^2 \theta_1 - \sin^2 \bar{\theta}_i^\pm}}{\sin^2 \bar{\theta}_i^\pm \cos \theta_1} \right). \quad (50)$$

In this case, the GH shift is given by

$$D_p^\pm = \frac{\lambda}{\pi} \frac{\sin \theta_1}{\sqrt{\sin^2 \theta_1 - \sin^2 \bar{\theta}_i^\pm}} h_\pm, \quad (51a)$$

$$h_\pm = \frac{\mu_1 \mu_2 \sin^2 \bar{\theta}_i^\pm \cos^2 \bar{\theta}_i^\pm}{\mu_1^2 \sin^4 \bar{\theta}_i^\pm \cos^2 \theta_1 + \mu_2^2 (\sin^2 \theta_1 - \sin^2 \bar{\theta}_i^\pm)}. \quad (51b)$$

The GH displacement per unit length in terms of the incidence angle is represented in Fig. 15.

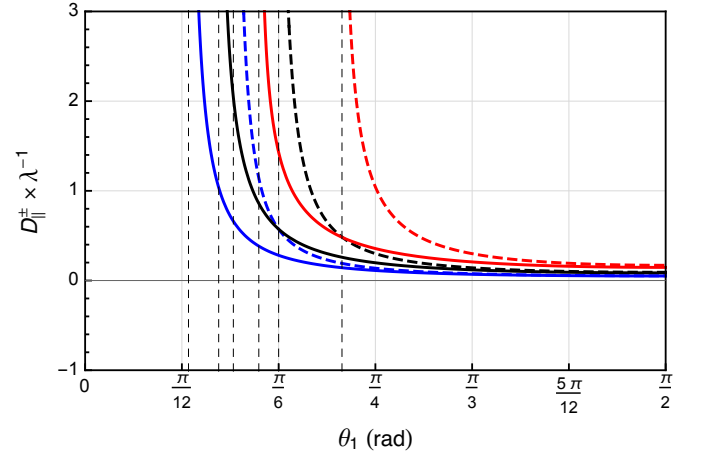


FIG. 15. Goos-Hänchen shift D_\parallel^+ (red lines) and D_\parallel^- (blue lines). Here, we have used: $\epsilon_1 = 4$, $\epsilon_2 = 1$, $\Sigma/\omega = 0.5$, $\mu_1 = \mu_2 = 1$ (dashed curves), and $\mu_1 = 2$, $\mu_2 = 1$ for solid lines. The black lines indicate the usual case ($\Sigma = 0$). The vertical dashed lines indicate the critical angle above which total internal reflection occurs for each example, accordingly to Eq. (46).

In general, Figures 14 and 15 indicate that the GH displacement for each propagating mode is shifted from the standard cases (black curves). On one hand, we observe that the magnetic conductivity Σ enables angles $\bar{\theta}_i^{\parallel, \pm}$ for total reflection smaller than the usual scenario, yielding, blue lines on the left of the black curves (usual case) in Figs. 15 and 14. On the other hand, the conductivity

Σ allows angles $\theta_+^{\parallel,\perp}$ for total reflection greater than the usual scenario, yielding the red lines on the right of the black curves (usual case) in Figs. 15 and 14.

B. Kerr rotation and Kerr ellipticity

As demonstrated in Eq. (12), the propagating modes in the dielectric substrate with magnetic current are given by LCP and RCP vectors. In this way, for a reflected wave in the surface of such a medium, the complex Kerr angle [28–30] is defined by

$$\tan \Phi_K = i \left(\frac{r_+ - r_-}{r_+ + r_-} \right), \quad (52)$$

where r_{\pm} are the complex Fresnel coefficients for LCP and RCP polarizations for normal incidence. Indeed, by considering normal incidence, $\theta_1 = 0$, one finds³

$$r_{\pm} = \frac{\mu_1 n_{2\pm} - \mu_2 n_1}{\mu_1 n_{2\pm} + \mu_2 n_1}. \quad (53)$$

Since the reflection coefficients are, in general, complex, the Kerr rotation angle (θ_K) and the Kerr ellipticity angle (η_K) are given by

$$\tan(2\theta_K) = -\frac{2\Delta''}{1 - |\Delta|^2}, \quad (54)$$

$$\sin(2\eta_K) = \frac{2\Delta'}{1 + |\Delta|^2}, \quad (55)$$

with $\Delta = \Delta' + i\Delta''$, where $\Delta' = \text{Re}[\Delta]$, $\Delta'' = \text{Im}[\Delta]$ and

$$\Delta = \frac{r_+ - r_-}{r_+ + r_-}. \quad (56)$$

In the small angle approximation [28, 29], one can also write

$$\theta_K = -\Delta'' = -\text{Im} \left(\frac{r_+ - r_-}{r_+ + r_-} \right), \quad (57)$$

$$\eta_K = \Delta' = \text{Re} \left(\frac{r_+ - r_-}{r_+ + r_-} \right), \quad (58)$$

which happens for most usual materials [39]. Implementing Eq. (53) in Eq. (56), it provides

$$\Delta = \frac{\mu_1 \mu_2 n_1 (n_{2+} - n_{2-})}{\mu_1^2 n_{2+} n_{2-} - \mu_2^2 n_1^2}. \quad (59)$$

³ We are considering the sign convention of Ref. [2, 61], where, at normal incidence, the reflection coefficient is that one obtained for an incident wave with p -polarization. This happens because, as pointed out in Refs. [1], at normal incidence there is no physical difference between s - and p -polarizations.

Replacing $n_1 = \sqrt{\mu_1 \epsilon_1}$ and Eq. (19) in Eq. (59), one finds

$$\Delta = \frac{\sqrt{\mu_1 \epsilon_1} \mu_2 \Sigma}{\mu_1 \epsilon_2 - \mu_2 \epsilon_1 \omega}. \quad (60)$$

Finally, by applying the real result (60) in Eq. (57) and Eq. (58), we obtain $\theta_K = 0$ and

$$\sin(2\eta_K) = \frac{2\sqrt{\mu_1 \epsilon_1} \mu_2 \Sigma}{\mu_1 \epsilon_2 - \mu_2 \epsilon_1 \omega} \frac{1}{1 + \frac{\mu_1 \epsilon_1}{(\mu_1 \epsilon_2 - \mu_2 \epsilon_1)^2} \left(\frac{\mu_2 \Sigma}{\omega} \right)^2}. \quad (61)$$

The latter represents a frequency-dependent ellipticity Kerr angle (a consequence of non-null magnetic conductivity Σ), which is illustrated in Fig. 16 in terms of the dimensionless parameter $x = \omega/\Sigma$. The maximum value of $\eta_{Kerr} = \pm\pi/4$ happens for specific values of frequency, given by

$$x^{\pm} = \frac{\mu_2 \sqrt{\mu_1 \epsilon_1}}{\pm \mu_1 \epsilon_2 \mp \mu_2 \epsilon_1}. \quad (62)$$

The plus (minus) sign of η_{Kerr} indicates the handedness of the reflected wave, which will be left- (right-) handed elliptically polarized [1]. The plus (minus) sign of x^{\pm} corresponds to the cases where $\mu_1 \epsilon_2 - \mu_2 \epsilon_1$ is positive (negative), which leads to $\eta_{Kerr} > 0$ ($\eta_{Kerr} < 0$). Furthermore, the possible maximum values for Kerr ellipticity are $\pm\pi/4$ regardless of the values of permeabilities (μ_1, μ_2) and permittivities (ϵ_1, ϵ_2). In the special case of $\mu_1 \epsilon_2 - \mu_2 \epsilon_1 = 0$, one finds $\eta_{Kerr} \rightarrow 0$, meaning that the reflected wave will be linearly polarized.

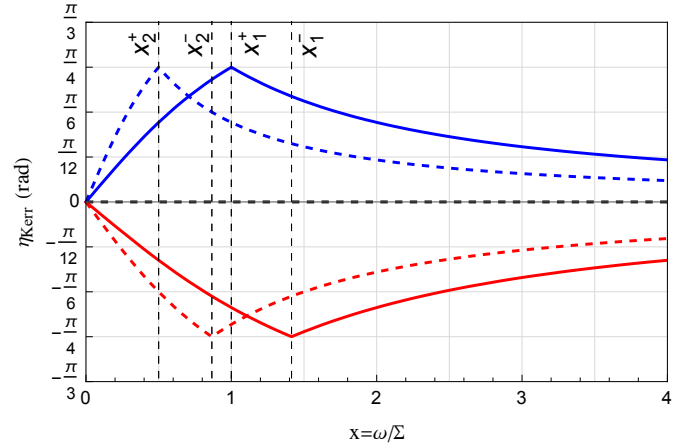


FIG. 16. Kerr ellipticity angle of Eq. (61). Here, we have used $\mu_1 = \mu_2 = 1$ for all curves. For solid blue (red) lines, we used: $\epsilon_1 = 1$, $\epsilon_2 = 2$ ($\epsilon_1 = 2$, $\epsilon_2 = 1$). For dashed blue (red) curves, we used: $\epsilon_1 = 1$, $\epsilon_2 = 3$ ($\epsilon_1 = 3$, $\epsilon_2 = 1$). The horizontal dashed black line represents the usual case ($\Sigma = 0$). The vertical dashed lines represent the values of x^{\pm} of Eq. (62) for each example.

In the very low-frequency regime, the Kerr ellipticity angle (61) behaves linearly with the frequency,

$$\eta_{Kerr}|_{low} \simeq \frac{\mu_1 \epsilon_2 - \mu_2 \epsilon_1}{\mu_2 \sqrt{\mu_1 \epsilon_1}} \frac{\omega}{\Sigma}, \quad (63)$$

while for very high frequencies it goes as

$$\eta_{Kerr}|_{high} \simeq \frac{\mu_2 \sqrt{\mu_1 \epsilon_1}}{\mu_1 \epsilon_2 - \mu_2 \epsilon_1} \frac{\Sigma}{\omega}. \quad (64)$$

We point out that the general frequency behavior of the Kerr ellipticity (61), depicted in Fig. 16, is analogous to the frequency-dependent Kerr effect observed in Weyl semimetals [40], where the optical activity is caused by the axion term. The evaluation of such an optical quantity in exotic materials endowed with magnetic conductivity may work as a tool to measure the magnitude of Σ .

VI. FINAL REMARKS

In this work, we have analyzed the reflection at the interface between an ordinary dielectric and a dielectric endowed with magnetic conductivity, starting from the Fresnel coefficients for s and p polarizations, presented in Eqs. (24) and (25), respectively.

For both polarizations, two frequency-dependent reflection coefficients were obtained, R^\pm , in considering the refractive indices n_+ and n_- . The behavior of the reflection coefficients was examined in terms of the incidence angle and frequency. The dispersive character is a novelty that brings several interesting new reflection properties.

For the polarization- s , the two reflection coefficients are R_\perp^\pm . As for R_\perp^+ , its magnitude decreases monotonically with the frequency, as depicted in Fig. 2 and Fig. 3. Its behavior with the incidence angle θ_1 is shown in Fig. 4, for a few values of Σ . All the coefficients R_\perp^+ increase continuously with the angle, while there occurs an overall magnitude enhancement with the value of Σ .

Concerning the reflection coefficient R_\perp^- , its behavior in terms of frequency is shown in Figs. 5 and 6, being substantially distinct from the one of R_\perp^+ . For non-null Σ values, the coefficient R_\perp^- becomes equal to 1 in the low-frequency interval $0 < \omega \leq \omega_i$, with ω_i given by Eq. (32), representing a scenario of total reflection induced by the dependence on the frequency of n_{2-} . Indeed, for $0 < \omega \leq \omega_i$, there occurs $n_{2-} < n_{1-}$, and the Snell's law explains the total reflection. An additional interesting property is the fact of $R_\perp^- = 0$ for a specific value of frequency, ω_0 , given by Eq. (33), as shown in Figs. 5 and 6, representing a partial Brewster angle for this polarization. The behavior of R_\perp^- in terms of the incidence angle θ_1 was also examined in Fig. 7, where regions of total reflection, $R_\perp^- = 1$, were reported for $\Sigma/\omega > 1$, being defined for $\bar{\theta}_i < \theta_1 < \pi/2$, with $\bar{\theta}_i$ given by Eq. (34). This total reflection region is also a consequence of the dispersive behavior of R_\perp^- , which does not occur in a conventional dielectric (see the dashed black line in Fig. 7).

For incident p -polarization, the reflection coefficients R_\parallel^\pm are given in Eq. (28). Figures 8 and 9 depict the reflectance R_\parallel^+ and R_\parallel^- , respectively, in terms of the

frequency, exhibiting behavior similar to the ones of s -polarization (in terms of the frequency). The behavior of R_\parallel^\pm with the incidence angle is illustrated in Figs. 10 and 11. The coefficient R_\parallel^+ , shown in Fig. 10, initially decreases with θ_1 , reaching a null value at the Brewster angle, and so augmenting its magnitude to the maximum value ($R_\parallel^+ = 1$). It differs from the R_\perp^+ behavior of Fig. 4), which rises up monotonically. In the case of R_\parallel^- , its behavior with θ_1 , given in Fig. 11, is nearly close to the profile of R_\perp^- of Fig. 7, both exhibiting a window of total reflection, $\bar{\theta}_i < \theta_1 < \pi/2$, with $\bar{\theta}_i$ given by Eq. (34).

The total reflection phenomenon can occur at the interface of Fig. 1 depending on the relations among the electromagnetic quantities describing the system. Each propagating mode can undergo total reflection according to the conditions presented in Tab. I, revealing that non-null magnetic conductivity increases the possibilities for this phenomenon to occur.

As for critical angles for null reflection, the general conditions for $R_{\perp,\parallel}^{\pm} = 0$ are presented in Tabs. II, III, V, and IV. For s -polarized incident wave, the same set of constitutive parameters does not yield simultaneously $R_\perp^+ = 0$ and $R_\perp^- = 0$. In this case, one has a specific critical angle at which $R_\perp^+ = 0$, $R_\perp^- \neq 0$ and another angle for $R_\perp^- = 0$, $R_\perp^+ \neq 0$. This is illustrated in Fig. 12. It defines the partial Brewster angles $\theta_{s\pm}^c$ of Eq. (39). On the other hand, for p -polarized incident wave, the critical angles for null reflection are given by Eq. (41). Considering the particular conditions adopted in rows c) of Tab. III and row d) of Tab. V, one can find a total Brewster angle $\theta_p|_{\bar{\omega}}$, with $\bar{\omega}$ given by Eq. (42). Also, from Fig. 13, we observe a total Brewster angle of $\pi/4$. Hence, a mixed incident wave with s and p polarization components becomes s -polarized upon incidence on the total Brewster angle $\theta_p|_{\bar{\omega}} = \pi/4$.

We have also shown that the GH displacement for each propagating mode is shifted from the standard cases, as illustrated in Figs. 14 and 15. The magnetic conductivity allows angles $\bar{\theta}_{\parallel,\perp}^{\pm}$ for total reflection smaller than the usual scenario, yielding GH blue lines on the left of the usual GH black curves in Figs. 15 and 14. Furthermore, the conductivity Σ allows angles $\bar{\theta}_{\parallel,\perp}^{\pm}$ for total reflection greater than the usual scenario, yielding the GH red lines on the right of the GH black lines in Figs. 15 and 14.

Another optical reflection signature of dielectric endowed with magnetic conductivity is the complex Kerr rotation, used to examine the reflected wave polarization upon normal incidence. We find a null Kerr rotation angle ($\theta_{Kerr} = 0$), while the Kerr ellipticity angle η_{Kerr} is given by Eq. (61), whose frequency-dependent behavior of η_{Kerr} is depicted in Fig. 16. An analogous dependence is also observed in Weyl semimetals, where the Kerr rotation is caused by axion terms. Thus, such reflection properties may provide a useful tool to optically probe the electromagnetic properties of chiral dielectric systems.

- [1] A. Zangwill, *Modern Electrodynamics*. New York (USA): Cambridge University Press, 2012.
- [2] J. D. Jackson, *Classical Electrodynamics*, 3rd edition. New York (USA): John Wiley & Sons, 1999.
- [3] A. H. Sihvola and I. V. Lindell, Properties of bi-isotropic Fresnel reflection coefficients, *Optics Communications* **89**, 1 (1992).
- [4] P. Hillion, Manifestly covariant formalism for electromagnetism in chiral media, *Phys. Rev. E* **47**, 1365 (1993).
- [5] Ming-Che Chang and Min-Fong Yang, Optical signature of topological insulators, *Phys. Rev. B* **80**, 113304 (2009).
- [6] Z.-W. Zuo, D.-B. Ling, L. Sheng, and D. Y. Xing, Optical properties for topological insulators with metamaterials, *Phys. Lett. A* **377**, 2909 (2013).
- [7] E. U. Condon, Theories of Optical Rotatory Power, *Rev. Mod. Phys.* **9**, 432 (1937).
- [8] H. S. Bennett, E. A. Stern, Faraday effect in solids. *Phys. Rev.* **137**, A448–A461 (1965); L. M. Roth. Theory of the Faraday effect in solids, *Phys. Rev.* **133**, A542–A553 (1964).
- [9] W. S. Porter and E. M. Bock Jr., Faraday effect in a plasma, *Am. J. Phys.* **33**, 1070 (1965).
- [10] M. P. Silverman; R. B. Sohn, Effects of circular birefringence on light propagation and reflection. *Am. J. Phys.* **54**, 69(1986).
- [11] D. G. Dimitriu, D. O. Dorohoi, New method to determine the optical rotatory dispersion of inorganic crystals applied to some samples of Carpathian Quartz, *Spectrochimica Acta Part A: Molecular and Biomolecular Spectroscopy* **131**, 674-677 (2014).
- [12] L.A. Pajdzik and A.M. Glazer, Three-dimensional birefringence imaging with a microscope tilting-stage. I. Uniaxial crystals, *J. Appl. Cryst.* **39**, 326 (2006).
- [13] X. Liu, J. Yang, Z. Geng, and H. Jia, Simultaneous measurement of optical rotation dispersion and absorption spectra for chiral substances, *Chirality* **8**, 32, 1071-1079 (2022).
- [14] L. D. Barron, *Molecular Light Scattering and Optical Activity*, 2nd ed. (Cambridge University Press, New York, 2004).
- [15] J.-M. Pouirol, P. Q. Liu, T. M. Slipchenko, A. Y. Nikitin, L. Martin-Moreno, J. Faist, and A. B. Kuzmenko, Electrically controlled terahertz magneto-optical phenomena in continuous and patterned graphene, *Nat Commun* **8**, 14626 (2017).
- [16] I. Tutunnikov, U. Steinitz, E. Gershnel, J.-M. Hartmann, A. A. Milner, V. Milner, and I. Sh. Averbukh, Rotation of the polarization of light as a tool for investigating the collisional transfer of angular momentum from rotating molecules to macroscopic gas flows, *Phys. Rev. Research* **4**, 013212 (2022); U. Steinitz and I. Sh. Averbukh, Giant polarization drag in a gas of molecular super-rotors, *Phys. Rev. A* **101**, 021404(R) (2020).
- [17] J. H. Woo, B. K. M. Gwon, J. H. Lee, D.-W. Kim, W. Jo, D. H. Kim, and J. W. Wu, Time-resolved pump-probe measurement of optical rotatory dispersion in chiral metamaterial, *Adv. Optical Mater.* **5**, 1700141 (2017).
- [18] Q. Zhang, E. Plum, J.-Y. Ou, H. Pi, J. Li, K. F. MacDonald, and N. I. Zheludev, Electrogyration in metamaterials: chirality and polarization rotatory power that depend on applied electric field, *Adv. Optical Mater.* **9**, 2001826 (2021).
- [19] J. Mun, *et al.* Electromagnetic chirality: from fundamentals to nontraditional chiroptical phenomena. *Light Sci. Appl.* **9**, 139 (2020).
- [20] J. Ma, and D. A. Pesin, Dynamic chiral magnetic effect and Faraday rotation in macroscopically disordered helical metals, *Phys. Rev. Lett.* **118**, 107401 (2017).
- [21] U. Dey, S. Nandy, and A. Taraphder, Dynamic chiral magnetic effect and anisotropic natural optical activity of tilted Weyl semimetals, *Sci Rep* **10**, 2699 (2020).
- [22] R. Gueroult, Y. Shi, J.-M. Rax, and N. J. Fisch, Determining the rotation direction in pulsars, *Nat. Commun.* **10**, 3232 (2019).
- [23] R. Gueroult, J.-M. Rax, and N. J. Fisch, Enhanced tunable rotatory power in a rotating plasma, *Phys. Rev. E* **102**, 051202(R) (2020).
- [24] F. S. Ribeiro, P. D. S. Silva, and M. M. Ferreira Jr, Cold plasma modes in the chiral Maxwell-Carroll-Field-Jackiw electrodynamics, *Phys. Rev. D* **bf107**, 096018 (2023).
- [25] F. S. Ribeiro, P. D. S. Silva, and M. M. Ferreira Jr, Anisotropic cold plasma modes in the chiral vector MCFJ electrodynamics, *Phys. Rev. D* **109**, 076003 (2024).
- [26] P. D. S. Silva and M. M. Ferreira Jr., Rotatory power reversal induced by magnetic current in bi-isotropic media, *Phys. Rev. B* **106**, 144430 (2022).
- [27] S. Miller, Y. Ding, L. Jiang, Xingzhou Tu, S. Pau, Observation of elliptically polarized light from total internal reflection in bubbles, *Sci. Rep.* **10**, 8725 (2020).
- [28] K. Shinagawa, in: *Solid-State Sciences: Magneto-Optics*, Vol. 128, Berlin: Springer-Verlag, 2000.
- [29] K. Sato and T. Ishibashi, Fundamentals of Magneto-Optical Spectroscopy, *Front. Phys.* **10**: 946515, (2022).
- [30] P. N. Argyres, Theory of the Faraday and Kerr Effects in Ferromagnetics, *Phys. Rev.* **97**, 334 (1955).
- [31] A. K. Bain, *Crystal Optics: Properties and Applications* (Wiley- VCH, Weinheim, Germany, 2019).
- [32] M. Kargarian, M. Randeria, and N. Trivedi, Theory of Kerr and Faraday rotations and linear dichroism in Topological Weyl Semimetals, *Sci. Rep.* **5**, 12683 (2015).
- [33] S. Ghosh, A. Sahoo, and S. Nandy, Theoretical investigations on Kerr and Faraday rotations in topological multi-Weyl semimetals, *SciPost Phys.* **15**, 133 (2023).
- [34] A. Sekine and K. Nomura, Axion electrodynamics in topological materials, *J. Appl. Phys.* **129**, 141101 (2021).
- [35] O. Trépanier, R. Duchesne, J. J. Boudreault, and R. Côté, Magneto-optical Kerr effect in Weyl semimetals with broken inversion and time-reversal symmetries, *Phys. Rev. B* **106**, 125104 (2022).
- [36] R. Côté, R. N. Duchesne, G. D. Duchesne, and O. Trépanier, Chiral filtration and Faraday rotation in multi-Weyl semimetals, *Results Phys.* **54**, 107064 (2023).
- [37] C. Guo, V. S. Asadchy, B. Zhao, and S. Fan, Light control with Weyl semimetals, *eLight* **3**, 2 (2023).
- [38] W.-K. Tse and A. H. MacDonald, Giant Magneto-Optical Kerr Effect and Universal Faraday Effect in Thin-Film Topological Insulators, *Phys. Rev. Lett.* **105**, 057401 (2010).
- [39] M. Schlenker and Y. Souche, in: *Magnetism: Fundamentals*, Boston (USA): Springer Science, 2005.
- [40] K. Sonowal, A. Singh, and A. Agarwal, Giant optical activity and Kerr effect in type-I and type-II Weyl semimet-

- als, *Phys. Rev. B* **100**, 085436 (2019).
- [41] T. Li, Y. Wang, Y. Jiang, S. Zhang, L. Luo, and Z. Zhang, High-precision measurement of the complex magneto-optical Kerr effect using weak measurement, *Appl. Phys. Lett.* **124**, 054001 (2024).
- [42] A. Kapitulnik, J. Xia, E. Schemm, and A. Palevski, Polar Kerr effect as probe for time-reversal symmetry breaking in unconventional superconductors, *New J. Phys.* **11**, 055060 (2009).
- [43] A. M.-Ruiz and C. A. Escobar, Casimir effect between ponderable media as modeled by the standard model extension, *Phys. Rev. D* **94**, 076010 (2016).
- [44] D.E. Kharzeev, The chiral magnetic effect and anomaly-induced transport, *Prog. Part. Nucl. Phys.* **75**, 133 (2014); D.E. Kharzeev, J. Liao, S.A. Voloshin, and G. Wang, Chiral magnetic and vortical effects in high-energy nuclear collisions – A status report, *Prog. Part. Nucl. Phys.* **88**, 1 (2016).
- [45] K. Fukushima, D.E. Kharzeev, and H.J. Warringa, Chiral magnetic effect, *Phys. Rev. D* **78**, 074033 (2008); D.E. Kharzeev and H. J. Warringa, Chiral magnetic conductivity, *Phys. Rev. D* **80**, 034028 (2009).
- [46] A. Vilenkin, Equilibrium parity-violating current in a magnetic field, *Phys. Rev. D* **22**, 3080 (1980); A. Vilenkin and D.A. Leahy, Parity nonconservation and the origin of cosmic magnetic fields, *Astrophys. J.* **254**, 77 (1982).
- [47] J. Schober, A. Brandenburg and I. Rogachevskii, Chiral fermion asymmetry in high-energy plasma simulations, *Geophys. Astrophys. Fluid Dynamics* **114**, 106 (2020).
- [48] M. Dvornikov and V.B. Semikoz, Influence of the turbulent motion on the chiral magnetic effect in the early universe, *Phys. Rev. D* **95**, 043538 (2017).
- [49] G. Sigl and N. Leite, Chiral magnetic effect in proton-neutron stars and magnetic field spectral evolution, *JCAP* **01**, 025 (2016).
- [50] M. Dvornikov and V.B. Semikoz, Magnetic field instability in a neutron star driven by the electroweak electron-nucleon interaction versus the chiral magnetic effect, *Phys. Rev. D* **91**, 061301(R) (2015).
- [51] M. Dvornikov and V.B. Semikoz, Instability of magnetic fields in electroweak plasma driven by neutrino asymmetries, *JCAP* **05**, 002 (2014); M. Dvornikov, Electric current induced by an external magnetic field in the presence of electroweak matter, *EPJ Web Conf.* **191**, 05008 (2018).
- [52] A.A. Burkov, Chiral anomaly and transport in Weyl metals, *J. Phys. Condens. Matter* **27**, 113201 (2015).
- [53] E. Barnes, J. J. Heremans, and Djordje Minic, Electromagnetic Signatures of the Chiral Anomaly in Weyl Semimetals, *Phys. Rev. Lett.* **117**, 217204 (2016).
- [54] X. Huang, L. Zhao, Y. Long, P. Wang, D. Chen, Z. Yang, H. Liang, M. Xue, H. Weng, Z. Fang, X. Dai, and G. Chen, Observation of the chiral-anomaly-induced negative magnetoresistance in 3D Weyl semimetal TaAs, *Phys. Rev. X* **5**, 031023 (2015).
- [55] Z. Qiu, G. Cao and X.-G. Huang, Electrodynamics of chiral matter, *Phys. Rev. D* **95**, 036002 (2017).
- [56] P. D. S. Silva, M. M. Ferreira Jr., M. Schreck, and L. F. Urrutia, Magnetic-conductivity effects on electromagnetic propagation in dispersive matter, *Phys. Rev. D* **102**, 076001 (2020).
- [57] P. D. S. Silva, M.J. Neves, M. M. Ferreira Jr., Optical properties and energy propagation in a dielectric medium supporting magnetic current, *Phys. Rev. B* **109**, 184439 (2024).
- [58] P. D. S. Silva, M.J. Neves, M. M. Ferreira Jr., Drude-Lorentz dielectric in the presence of a magnetic current density., *Phys. Rev. B* **109**, 184444 (2024).
- [59] P. D. S. Silva, L. Lisboa-Santos, M. M. Ferreira Jr., and M. Schreck, Effects of *CPT*-odd terms of dimensions three and five on electromagnetic propagation in continuous matter, *Phys. Rev. D* **104**, 116023 (2021).
- [60] G. R. Fowles, *Introduction to modern optics*, 2nd ed. (Dover Publications, INC., New York, 1975).
- [61] E. Hecht, *Optics*, 4th ed. (Addison Wesley, San Francisco, 2002).
- [62] S.M. Carroll, G.B. Field, and R. Jackiw, Limits on a Lorentz- and parity-violating modification of electrodynamics, *Phys. Rev. D* **41**, 1231 (1990).
- [63] D. Colladay and V.A. Kostelecký, *CPT* violation and the standard model, *Phys. Rev. D* **55**, 6760 (1997); D. Colladay and V.A. Kostelecký, Lorentz-violating extension of the standard model, *Phys. Rev. D* **58**, 116002 (1998).
- [64] K. Deng, J. S. Van Dyke, D. Minic, J. J. Heremans, and E. Barnes, Exploring self-consistency of the equations of axion electrodynamics in Weyl semimetals, *Phys. Rev. B* **104**, 075202 (2021).
- [65] F. Wilczek, Two Applications of Axion Electrodynamics, *Phys. Rev. Lett.* **58**, 1799 (1987).
- [66] A. Sekine and K. Nomura, Axion electrodynamics in topological materials, *J. Appl. Phys.* **129**, 141101 (2021).
- [67] M. E. Tobar, B. T. McAllister, and M. Goryachev, Modified axion electrodynamics as impressed electromagnetic sources through oscillating background polarization and magnetization, *Phys. Dark Universe* **26**, 100339 (2019).
- [68] Z. Qiu, G. Cao and X.-G. Huang, Electrodynamics of chiral matter, *Phys. Rev. D* **95**, 036002 (2017).
- [69] A. Gomez, A. Martín-Ruiz, Luis F. Urrutia, Effective electromagnetic actions for Lorentz violating theories exhibiting the axial anomaly, *Phys. Lett. B* **829**, 137043 (2022).
- [70] A.Gómez, R. M. von Dossow, A. Martín-Ruiz, L. F. Urrutia, Lorentz invariance violation and the *CPT*-odd electromagnetic response of a tilted anisotropic Weyl semimetal, *Phys. Rev. D* **109**, 065005 (2024).
- [71] A. V. Kostelecky, R. Lehnert, N. McGinnis, M. Schreck, B. Seradjeh, Lorentz violation in Dirac and Weyl semimetals, *Phys. Rev. Research* **4**, 023106 (2022).
- [72] A. Martín-Ruiz and C. A. Escobar, Casimir effect between ponderable media as modeled by the standard model extension, *Phys. Rev. D* **94**, 076010 (2016); A. Martín-Ruiz and C. A. Escobar, Local effects of the quantum vacuum in Lorentz-violating electrodynamics, *Phys. Rev. D* **95**, 036011 (2017).
- [73] E. Barredo-Alamilla, Daniel A. Bobylev, and Maxim A. Gorlach, Axion electrodynamics without Witten effect in metamaterials, *Phys. Rev. B* **109**, 195136 (2024).
- [74] A. H. Sihvola and I. V. Lindell, Novel effects in wave reflection from biisotropic media, *Microw. Opt. Technol. Lett.* **6**, 581–585 (1993).
- [75] A. Kumar and A. Ghatak, *Polarization of Light with Applications in Optical Fibers*, SPIE: Bellingham, Washington (USA), 2011.
- [76] J.-F. Wu and Y.-T. Zhang, The relation between the propagation of extraordinary ray and the optical axis in the uniaxial crystal, *Optik* **124**, 2667-2669 (2013).